A metamaterial sensor for detecting the location of a sub-wavelength object

Yujie Hua, Wenxuan Tang and Tie Jun Cui

View Online

Export Citation

CrossMark

ARTICLES YOU MAY BE INTERESTED IN

Broadband spin-unlocked metasurfaces for bifunctional wavefront manipulations
Applied Physics Letters **120**, 181702 (2022); https://doi.org/10.1063/5.0091051

Nondestructive inspection of metallic microstructure chips based on photoacoustic remote sensing microscopy
Applied Physics Letters **120**, 182201 (2022); https://doi.org/10.1063/5.0090897

Broadband terahertz time-domain polarimetry based on air plasma filament emissions and spinning electro-optic sampling in GaP
Applied Physics Letters **120**, 181107 (2022); https://doi.org/10.1063/5.0087127

A metamaterial sensor for detecting the location of a sub-wavelength object

View Online   Export Citation   CrossMark

Yujie Hua,[1,2] iD Wenxuan Tang,[1,2,a] iD and Tie Jun Cui[1,2,a] iD

AFFILIATIONS

[1]State Key Laboratory of Millimeter Waves, School of Information Science and Engineering, Southeast University, Nanjing 210096, People's Republic of China
[2]Institute of Electromagnetic Space, Southeast University, Nanjing 210096, China

[a]Authors to whom correspondence should be addressed: wenxuant@seu.edu.cn; and tjcui@seu.edu.cn

ABSTRACT

A metamaterial sensor is proposed to detect the random location of a sub-wavelength metallic object. The sensor is composed of a transmission line (TL), which supports the propagation of spoof surface plasmon polaritons (SSPPs) with localized electromagnetic (EM) field, and a complementary spiral resonator (CSR) that resonates strongly at designed frequencies around 0.9 and 2.7 GHz. Based on the shift of the resonance frequencies, this sensor is able to detect the location of a sub-wavelength metallic object (whose diameter is smaller than 0.6 mm) randomly attached to the CSR. A prototype of the sensor is fabricated and tested. In practice, the CSR is excited through the EM coupling of the SSPP TL, and the location of the metallic object is obtained through the transmission coefficient (S21). To improve the accuracy, a retrieval curve for locating is generated and calibrated. It is proved that the random location of the sub-wavelength object can be accurately detected inside an area of 9π mm^2 with a low error of 2‰.

Published under an exclusive license by AIP Publishing. https://doi.org/10.1063/5.0090146

With the vigorous development of the Internet of Things (IoT) and the increasing application of wearable devices, the demand for sensors is expanding.[1] Flexible and wearable systems are utilized to monitor inflammatory skin diseases,[2] detect human body temperature,[3] analyze sweating rate,[3,4] etc. Microwave sensors based on electromagnetic (EM) resonance have become an important solution due to the virtue of low cost, high sensitivity, and robustness to harsh environments.[1] Nowadays, sensors that adopt the microwave principle have been developed quickly, including those for detecting the characterization of materials,[5,6] concentration of solution,[6–9] properties of microfluidic,[10,11] image,[12] pressure,[13] temperature,[14,15] and angular displacement.[16–18]

In recent years, metamaterial sensors have been investigated because their designable resonances may result in novel functions and outstanding performances. Among them, the spoof surface plasmon polaritons (SPPs) and localized surface plasmons[19–21] (LSPs), which are considered as the plasmonic metamaterials, are especially suitable to compose sensors due to their localized EM fields, high quality factor (Q-value), low and conformal profiles, and easy integration in flexible circuits. An ultrafast and high-sensitivity humidity sensor was fabricated to quantify the humidity using the spoof LSP device.[22] A microfluidic chemical sensor was created based on quarter-mode spoof LSPs to possess the merits of high sensitivity, compact size, and very low requirement of testing liquid.[23] A dielectric sensor that takes advantage

of spoof surface plasmon polaritons (SSPPs) was presented to easily integrate in microwave and THz systems.[5] In addition, angular displacement sensors are also available. One of the designs was based on a rotor comprised of a complementary split-ring resonator (CSRR) placed on the ground plane of the microstrip line, and the detectable angular displacement ranges from 0° to 90°.[16] When a rotational cross-shaped resonator (RCSR) was used, the sensor was able to detect the angular displacement from −180° to 180°.[17] However, although the sensors can accurately detect the angular displacement of the object, few sensors can detect the precise position of the object, especially for electrically small objects. The spiral EM resonators, which possess simple structures and high Q resonances,[24–26] have the polar coordinate angle to represent location information and, therefore, are good candidates for location sensing.

In this work, we propose a microwave sensor for detecting the location of a sub-wavelength metallic object. The sensor is made of a complementary spiral resonator (CSR) and a SSPP TL. The CSR is pierced in the ground of the SSPP TL for strong EM coupling and compact configuration. When a metallic object is added on the CSR, the resonance frequency changes in line with the location of the object because it terminates the resonating current in the CSR. Change of the resonance is observed through the shift of transmission zero of the SSPP TL. The relationship between the resonance frequency and the

location of the metallic object is analyzed theoretically, retrieved numerically, and demonstrated experimentally.

The proposed sensor is composed of the SSPP TL on the top of the dielectric substrate and the CSR on the ground [Figs. 1(a) and 1(b)]. The TL is used to support the propagation of SSPPs, which is a type of slow wave. Figure 2 shows the dispersion diagram of the SSPP TL and the geometric parameters. The dispersion curve gradually departs to the right side, resulting in a cutoff frequency beyond which the SSPP waves cannot propagate. In this work, the cutoff frequency is designed to 8 GHz, which is far away from the resonance frequencies of the CSR. The SSPP TL is fed with microstrip lines in Sec. I (defined in Fig. 1). Gradient strips are added in Sec. II for impedance and momentum matching between the microstrip line and the uniform SSPP structure in Sec. III. It has been demonstrated that the SSPP TL possesses stronger field confinement when compared with the microstrip line.[27] Therefore, the CSR can be intensively stimulated due to the strong EM coupling. Electric currents are induced and resonate in the sculptured spiral-shape hollow at specific frequencies, resulting in transmission zeros where the EM energy cannot propagate on the TL.

In this design, the CSR shown in Fig. 1(c) has a diameter of 6 mm and is described as

$$\begin{cases} X_1 = r * r_n * \cos(r_n * \pi), \\ Y_1 = r * r_n * \sin(r_n * \pi), \end{cases} \quad \text{where } 0 < r_n < r_x. \quad (1)$$

Here, $r = 0.2$, $r_x = 14$, and X_1 is the x coordinate of the spiral curve and Y_1 is the y coordinate. Figure 1(d) shows a metallic object placed on the CSR. The width of the sculptured spiral-shape hollow is 0.2 mm. So, as long as the metallic object has a diameter between 0.4 mm and 0.6 mm, it can block one hollow, can change the length of the resonating electric currents in the CSR, and, consequently, change the resonance frequencies. The rotation angle θ in the polar coordinate can be used to uniquely determine the location of the metallic object as

$$\begin{cases} X = r * \left(\dfrac{\theta}{360} + 1\right) * \cos\left(\left(\dfrac{\theta}{360} + 1\right) * \pi - 0.5 * \pi\right), \\ Y = r * \left(\dfrac{\theta}{360} + 1\right) * \sin\left(\left(\dfrac{\theta}{360} + 1\right) * \pi - 0.5 * \pi\right), \\ \text{where } 0° < \theta < 4800°. \end{cases} \quad (2)$$

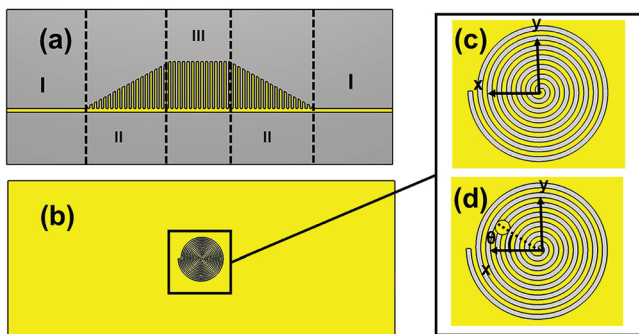In this work, θ ranges from 0° to 4800°.

FIG. 1. (a) Top view and (b) bottom view of the proposed sensor. (c) The CSR (zoomed out). (d) The CSR with a metallic object located on it. The yellow part is metal (copper) and the gray one is dielectric (Rogers 4350).
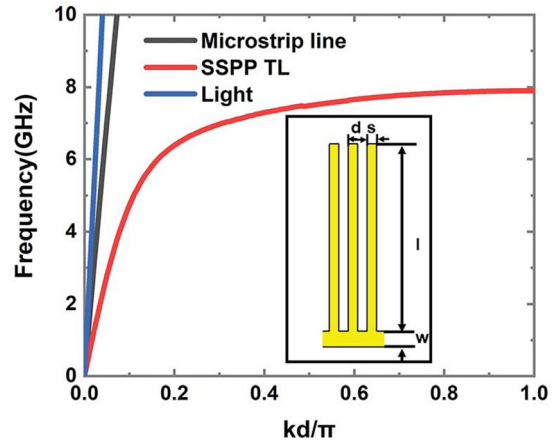

FIG. 2. Dispersion diagram of the SSPP TL. Inset: the SSPP units, in which $d = 0.6$ mm, $w = 0.5$ mm, $l = 6$ mm, and $s = 0.3$ mm.

When the metallic object is added to the CSR, there exist multiple resonant modes. For the sake of easy application, only the first two resonant modes are chosen for analysis. Figure 3 shows the normalized amplitudes of magnetic fields for the two resonant modes when the metallic object is located at different locations. Generally, the location of the metallic object is categorized into four regions in correspondence with θ. Figure 3(a) shows the magnetic field distribution when the metallic object is located within the first region where $0° < \theta < 2460°$ (region I). It is observed that the fields resonate in different manners in Figs. 3(a1) and 3(a2), resulting in the first and second orders of resonant mode (named as "mode 1" and "mode 2"). Note that, in this case, since the inner branch (from the metallic object to the center of the spiral) is very short, both the first and second resonances occur in the outer branch (from the metallic object to the outer end of the spiral). Obviously, mode 1 is generated when the current path is comparable to the wavelength, and mode 2 is generated when the current path is twice of the wavelength. Figure 3(b) shows that when the metallic object is located within the second region where $2460° < \theta < 3480°$ (region II), mode 1 is determined by the resonance in the outer branch, while mode 2 is determined by the resonance in the inner branch. This is because the current path of the inner branch is long enough to generate the second resonance. When the metallic object is located in the third region where $3480° < \theta < 4110°$ (region III) and in the fourth region where $4110° < \theta < 4800°$ (region IV), two resonant modes are also observed according to the distributions of the magnetic fields. We denote that higher order resonances can be even observed and included to improve the sensing performance in more rigorous scenarios.[28]

When the CSR is excited by the SSPP TL through near-field coupling, most energy radiates to the free space, and transmission zeros appear at resonance frequencies. Figure 4 plots the simulated S21 curves when the metallic object is at different locations. Figure 4(a) shows that when the metallic object is located in region I, the resonance frequencies of mode 1 and mode 2 increase monotonously as the angle θ increases. This is because when θ increases from 0°, the metallic object moves from the center of the spiral toward the outer end, and the resonating branch becomes shorter and the resonance
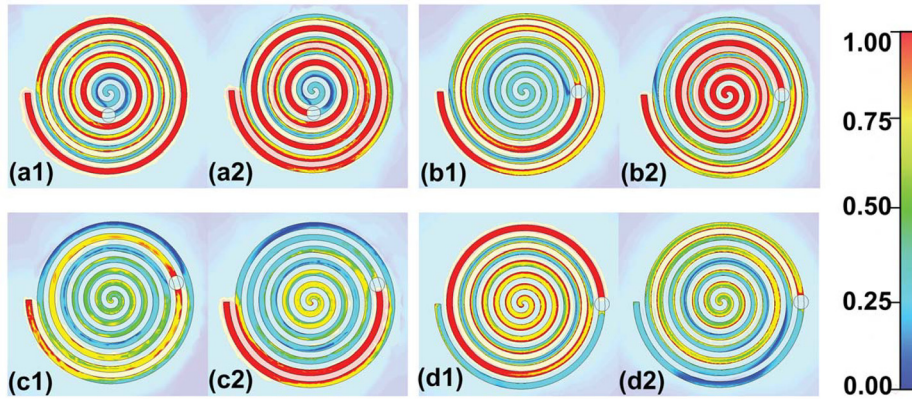
FIG. 3. The normalized magnitudes of the magnetic fields at resonance frequencies. (a1) Mode 1 and (a2) mode 2 in region I; (b1) mode 1 and (b2) mode 2 in region II; (c1) mode 1 and (c2) mode 2 in region III; and (d1) mode 1 and (d2) mode 2 in region IV.

frequency goes higher accordingly. Figure 4(b) shows that when it is in region II, the frequency of mode 1 continues to increase monotonously but that of mode 2 decreases monotonously, due to the reason that the resonance of mode 2 happens on the inner branch. As the metallic object continues to move to the outer end of the spiral, the length of the inner branch increases and that of the outer branch decreases. However, in region III, the frequency of mode 1 varies only slightly, as is plotted in the inset of Fig. 4(c), indicating a low resolution of the sensor. In other

words, it is hard to decide the location of the metallic object by only detecting the change of mode 1. Fortunately, the change of the frequency of mode 2 is significant, which is due to the fact that the resonance in the outer branch is intense [as indicated in Fig. 3(c)]. In view of this, one is able to detect the angular displacement of the object by observing the change of mode 1 and mode 2 together. Figure 4(c) shows that, in this region, the frequency of mode 1 decreases slowly and that of mode 2 increases quickly as θ goes higher. In region IV, the resonances
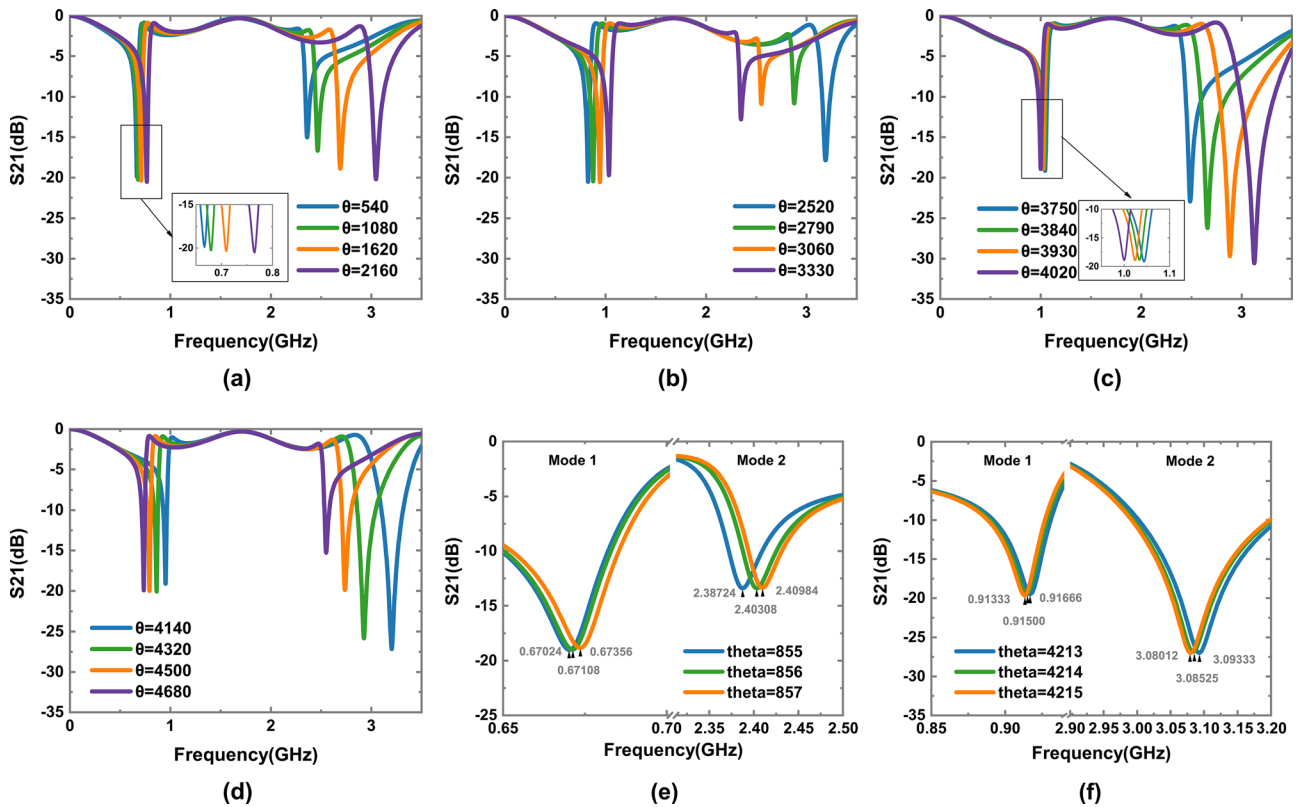

FIG. 4. (a)–(f) Simulated S21 when the metallic object is placed in different areas with regard to the coordinate angle θ. (a) $0° < \theta < 2460°$, (b) $2460° < \theta < 3480°$, (c) $3480° < \theta < 4110°$, and (d) $4110° < \theta < 4800°$. (e) Angular resolution around $\theta = 856°$ and (f) $\theta = 4214°$.

at mode 1 and mode 2 both happen in the inner branch, and therefore, both the resonance frequencies decrease monotonically as θ increases. Through the above analysis, it is discovered that there is a correspondence between the location of the metallic object and the resonance frequencies of the first two modes. Moreover, high resolution can be guaranteed in different areas of polar coordinates, as indicated in Figs. 4(e)–4(f). When θ varies with $1°$ shift, the frequency resolution is 0.001 GHz for mode 1 and 0.005 GHz for mode 2 in region I and is 0.0015 GHz for mode 1 and 0.005 GHz for mode 2 in region IV. Assuming that the testing equipment has a frequency resolution of 0.001 GHz, it can guarantee the angular resolution of $1°$ (around $856°$) and $0.6°$ (around $4214°$) through measuring the first resonance frequency, and the corresponding distance resolutions are about 0.005 92 and 0.0133 mm, respectively, both in the deep sub-wavelength scale.
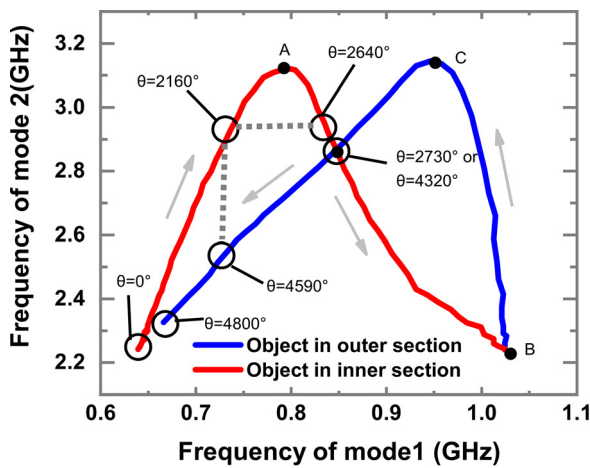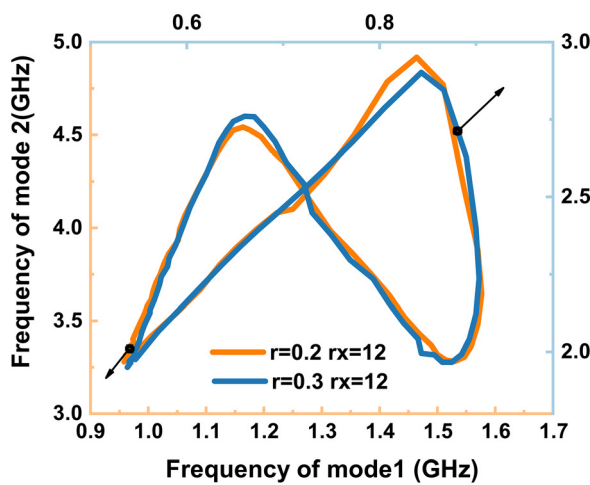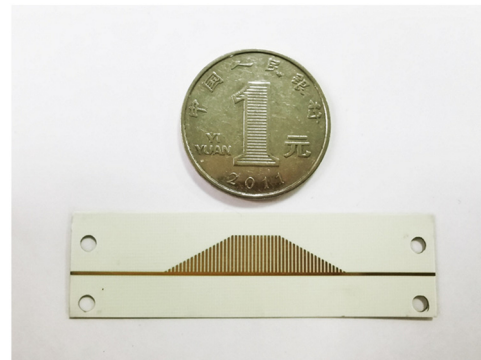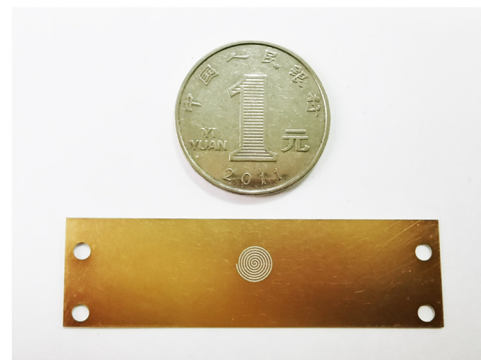
Based on the simulated results, Fig. 5 plots the fitting curves of the two resonance frequencies when θ increases from $0°$ to $4800°$. The red curve starts from $\theta = 0°$ and ends at $\theta = 3480°$ (point B), indicating that the metallic object is located in the inner section. The blue one starts from point B and ends at $\theta = 4800°$, indicating that the metallic object is in the outer section. When the metallic object moves from the center, θ increases continuously from $0°$, and the frequencies of mode 1 and mode 2 increase monotonously until point A ($\theta = 2460°$). As θ keeps increasing, the frequency of mode 1 increases monotonously but that of mode 2 begins to decrease. There is another inflexion at point B, from which the metallic object moves to the outer section. When θ increases from point B to point C ($\theta = 4110°$), the frequency of mode 1 increases monotonously but that of mode 2 decreases. Beyond point C, both frequencies decrease monotonously. From Fig. 5(a), it is concluded that there is a one-to-one correspondence between the frequencies of mode 1 and mode 2 and the angular of θ. The only exception happens at point D where θ may be either $2730°$ or $4320°$. Solution to this problem will be discussed in the following text. In addition, to verify the scalability and applicability of this scheme, we scale down the CSR with r = 0.2 and $r_x = 12$ and scale it up with r = 0.3 and $r_x = 12$ and plotted the corresponding resonance frequencies in Fig. 5(b). It is shown that the larger CSR results in the lower resonance frequencies (see the blue curve) and vice versa (see the orange curve). Therefore, the proposed scheme can work when the CSR is scaled up with more turns or larger linewidth, or scaled down in the opposite way. As long

(a)

(b)

FIG. 5. (a) Relationship between the resonance frequencies and θ when r = 0.2 and $r_x = 14$. (b) Relationship between the resonance frequencies and θ when the CSR is scaled in terms of r and r_x.

(a)

(b)

FIG. 6. (a) Top view and (b) bottom view of the prototype.

as the linewidth is fine enough, the sensor can maintain its function and deep sub-wavelength resolution after scaling.

The above designed sensor is fabricated, and the photo of the prototype is given in Fig. 6. The white part is the substrate (thickness = 0.254 mm, ε_r = 3.66, and loss tangent = 0.0037), and the yellow part is the 0.035-mm-thick copper. The four through holes in the corners are used to fix the SMA connector to connect with the coaxial cables from the vector network analyzer (VNA). In order to test the sensor, we locate the sub-wavelength metallic object at five different positions, including θ = 2160°, θ = 2640°, θ = 2730°, θ = 4320°, and θ = 4590°. It is observed that at θ = 2160° and θ = 2640°, the frequencies of mode 2 are same, while that of mode 1 are different, and at θ = 2160° and θ = 4590°, the frequencies of mode 1 are same, while that of mode 2 are different. Moreover, as is pointed out above, the frequencies of mode 1 and mode 2 are identical at θ = 2730° and θ = 4320°.

Figure 7(a) compares the measured and simulated S21 when θ = 2160° and θ = 2640°. The frequencies of mode 2 are almost the same, while the position can be distinguished by the frequency of mode 1, which is consistent with the simulated result. The comparison of measured and simulated S21 when θ = 2160° or θ = 4590° is shown in Fig. 7(b). Clearly, the position can be determined by the frequency of mode 2 regardless of the similar frequencies of mode 1. Additionally, as mentioned above, there are two locations (θ = 2730° and θ = 4320°) where the resonance frequencies of the two modes are

nearly identical, as is shown in Fig. 7(c). However, the resonance of mode 2 at θ = 4320° is much stronger than that at θ = 2730°. In particular, as is shown in Fig. 7(c), when θ = 4320°, the resonance at mode 2 is comparable to that at mode 1, with the valley values of S21 being about −20 dB in measurement. In contrast, when θ = 2730°, the resonance at mode 2 is much weaker than that at mode 1, resulting in the valley value of S21 around −10 dB in measurement. In other words, one is able to distinguish the two positions by comparing the intensities of the two resonances. Therefore, the proposed sensor is able to detect the unique location of the sub-wavelength metallic object.

It should be pointed out that because of the errors in fabrication and assembly, there is a slight linear shift of frequency between the simulated and the measured results. Figure 7 indicates that the frequency shift of mode 1 is less than 0.025 GHz and that of mode 2 is less than 0.08 GHz. Therefore, corrective actions are necessary to ensure the performance of the sensor. In this work, the measured values of S21 at θ = 2160°, 2640°, and 4590° are chosen to calibrate the simulated fitting curve in Fig. 5. The mean value of the frequency deviation at the three points is used as the calibration error. The scatter point connection line after calibration is shown as the black curve in Fig. 7(d), where the x-axis and y-axis record the resonance frequencies of mode 1 and mode 2 respectively, and the z-axis is the angular position in the term of θ. The red, blue, and green lines are the projections in the xoz, yoz, and xoz planes, respectively. One is able to determine
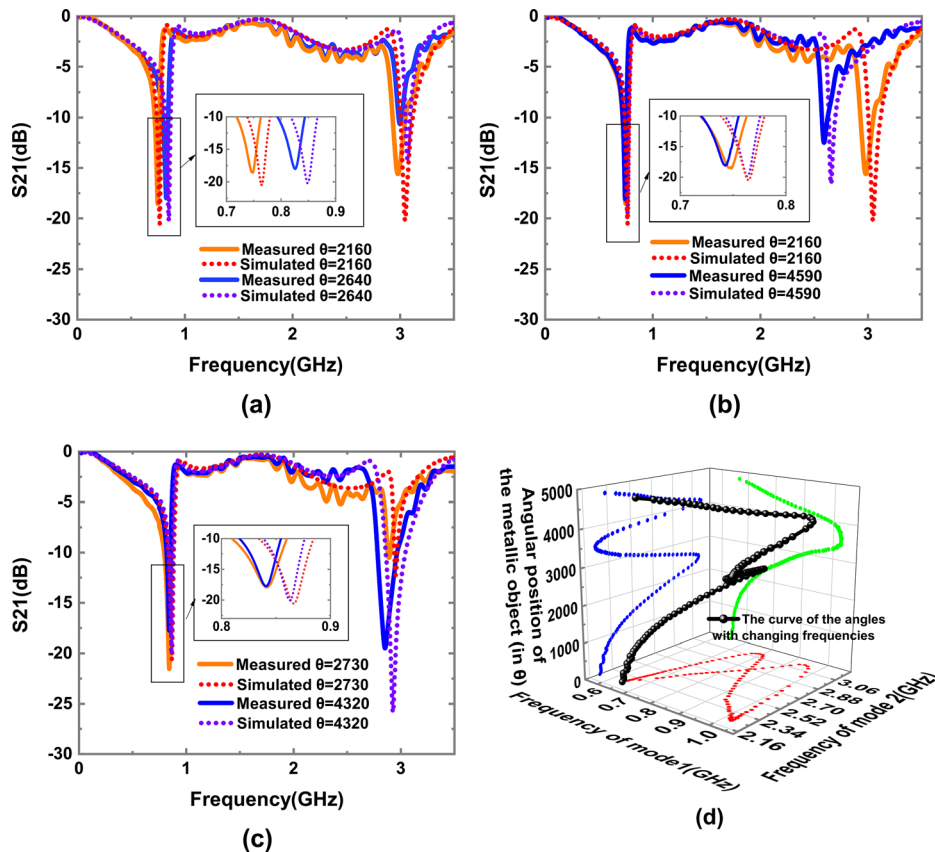

FIG. 7. (a)–(c) Simulated and measured S21 when the metallic object is at different locations. (d) The calibrated scatter point connection line for location retrieval.

the exact position of an unknown metallic object by measuring the first two resonance frequencies and retrieving the value of θ in the scatter point connection line given in Fig. 7(d).

For demonstration, we tested two samples. The first sample has the metallic object located at $\theta = 2730°$, and the two resonances are found at 0.8414 and 2.8918 GHz. The correspondingly retrieved angle is $\theta = 2715°$. The second sample has the metallic object located at $\theta = 4320°$, and the two resonances are found at 0.8408 and 2.8534 GHz. The correspondingly retrieved angle is $\theta = 4330°$. When the angle values are substituted into Eq. (2), the errors of location are less than 0.2 mm, which is 2‰ λ_0 at 3 GHz. Therefore, the sensor is verified to detect the location of a sub-wavelength object with the error of 2‰.

In summary, a microwave sensor has been proposed to detect the location of a sub-wavelength metallic object with high accuracy and resolution. Prototypes composed of the SSPP TLs and CSRs have been designed, fabricated, and tested. From simulation and measurement, it is verified that the location of the metallic object can be uniquely determined by simply measuring the S21 parameters. This metamaterial sensor possesses high accuracy, high resolution, low profile, and low cost and, hence, can be adopted as an efficient method for microwave sensing in different application scenarios such as meter measuring in the automotive industry[29] and fabrication of precision instruments.

AUTHOR DECLARATIONS
Conflict of Interest

The authors have no conflicts to disclose.

DATA AVAILABILITY

The data that support the findings of this study are available from the corresponding authors upon reasonable request.

REFERENCES

[1]F. Martin, P. Velez, and M. Gil, Sensors **20**, 3375 (2020).
[2]S. R. Madhvapathy, H. Wang, J. Kong, M. Zhang, J. Y. Lee, J. B. Park, H. Jang, Z. Xie, J. Cao, R. Avila, C. Wei, V. D'Angelo, J. Zhu, H. U. Chung, S. Coughlin, M. Patel, J. Winograd, J. Lim, A. Banks, S. Xu, Y. Huang, and J. A. Rogers, Sci. Adv. **6**, eabd714 (2020).
[3]Y. Jiang, K. Pan, T. Leng, and Z. Hu, IEEE J. Electromagn. RF Microwaves Med. Biol. **4**, 164 (2020).
[4]L. B. Baker, J. B. Model, K. A. Barnes, M. L. Anderson, S. P. Lee, K. A. Lee, S. D. Brown, A. J. Reimel, R. Ghaffari, J. A. Rogers, A. J. Aranyosi, J. T. Reeder, M. S. Seib, W. Li, J. M. Carter, C. T. Ungaro, J. L. Bonsignore, R. P. Nuccio, and T. J. Roberts, Sci. Adv. **6**, eabe3929 (2020).
[5]S. P. Singh, N. K. Tiwari, and M. J. Akhtar, IEEE Sens. J. **20**, 193 (2020).
[6]E. L. Chuma, Y. Iano, G. Fontgalland, and L. L. Bravo Roger, IEEE Sens. J. **18**, 9978 (2018).
[7]Y. J. Zhou, Q. Y. Li, H. Z. Zhao, and T. J. Cui, Adv. Mater. Technol. **5**, 1900767 (2020).
[8]M. N. Rahman, S. A. Hassan, M. Samsuzzaman, M. S. J. Singh, and M. T. Islam, Microwave Opt. Technol. Lett. **61**, 361 (2019).
[9]Y. Yan, X. Lin, Z. Chen, Y. Cai, and Z. Chen, in IEEE Asia-Pacific Microwave Conference, 2020, Vol. 427.
[10]H. Z. Zhao, Y. J. Zhou, J. Cai, Q. Y. Li, and Z. Y. Xiao, J. Phys. D **53**, 095305 (2020).
[11]K. Malecha, L. Jasinska, A. Grytsko, K. Drzozga, P. Słobodzian, and J. Cabaj, Sensors **19**, 577 (2019).
[12]L. Wang, Sensors **18**, 655 (2018).
[13]A. A. Shamabadi, M. Rezaee, and A. Kazemi-Beydokhti, Microwave Opt. Technol. Lett. **62**, 2821 (2020).
[14]F. Lu, Q. Tan, Y. Ji, Q. Guo, Y. Guo, and J. Xiong, Sensors **18**, 2879 (2018).
[15]X. Ren, S. Ebadi, Y. Chen, L. An, and X. Gong, IEEE Trans. Microwave Theory Tech. **61**, 960 (2013).
[16]A. K. Jha, N. Delmonte, A. Lamecki, M. Mrozowski, and M. Bozzi, IEEE Microwave Wireless Compon. Lett. **29**, 306 (2019).
[17]C. Teng, C. H. Chio, K. W. Tam, and P. Y. Lau, IEEE Sens. J. **21**, 2899 (2021).
[18]J. Naqui and F. Martín, IEEE Sens. J. **14**, 939 (2014).
[19]F. Gao, Z. Gao, Y. Luo, and B. Zhang, Adv. Funct. Mater. **26**, 8307–8312 (2016).
[20]J. Zhang, Z. Liao, Y. Luo, X. Shen, S. A. Maier, and T. J. Cui, Laser Photonics Rev. **11**, 1600191 (2017).
[21]Z. Li, Z. Li, L. Liu, A. I. Fernández-Domínguez, J. Shi, C. Gu, F. J. García-Vidal, Y. Luo et.al., Adv. Opt. Mater. **7**, 1900118 (2019).
[22]H. Yu, C. Wang, F. Y. Meng, J. G. Liang, H. S. Kashan, K. K. Adhikari, L. Wang, E. S. Kim, and N. Y. Kim, Sens. Actuators, B **304**, 127138 (2020).
[23]R. L. Rong, Y. J. Zhou, and L. Yang, Appl. Opt. **57**, 8472 (2018).
[24]Z. Liao, G. Q. Luo, H. F. Ma, B. C. Pan, B. G. Cai, Y. F. Yu, and T. J. Cui, Phys. Rev. Appl. **10**, 034054 (2018).
[25]P. A. Huidobro, X. P. Shen, J. Cuerda, E. Moreno, L. Martin-Moreno, F. J. Garcia-Vidal, T. J. Cui, and J. B. Pendry, Phys. Rev. X **4**, 021003 (2014).
[26]W. Tang, Y. Hua, and T. J. Cui, Electronics **10**, 4 (2020).
[27]H. C. Zhang, Q. Zhang, J. F. Liu, W. Tang, Y. Fan, and T. J. Cui, Sci. Rep. **6**, 23396 (2016).
[28]Z. Liao, Y. Luo, A. I. Fernández-Domínguez, X. Shen, S. A. Maier, and T. J. Cui, Sci. Rep. **5**, 9590 (2015).
[29]W. Gannouni, M. L. Doumbia, and A. Badri, Microelectron. Eng. **236**, 111480 (2021).